RESEARCH ARTICLE

Fast and Durable Lithium Storage Enabled by Tuning Entropy in Wadsley–Roth Phase Titanium Niobium Oxides

Jie Zheng, Rui Xia, Congli Sun, Najma Yaqoob, Qianyuan Qiu, Liping Zhong, Yongdan Li, Payam Kaghazchi, Kangning Zhao,* Johan E. ten Elshof, and Mark Huijben*

Wadsley–Roth phase titanium niobium oxides have received considerable interest as anodes for lithium ion batteries. However, the volume expansion and sluggish ion/electron transport kinetics retard its application in grid scale. Here, fast and durable lithium storage in entropy-stabilized $Fe_{0.4}Ti_{1.6}Nb_{10}O_{28.8}$ (FTNO) is enabled by tuning entropy via Fe substitution. By increasing the entropy, a reduction of the calcination temperature to form a phase pure material is achieved, leading to a reduced grain size and, therefore, a shortening of Li^+ pathway along the diffusion channels. Furthermore, in situ X-ray diffraction reveals that the increased entropy leads to the decreased expansion along a–axis, which stabilizes the lithium intercalation channel. Density functional theory modeling indicates the origin to be the more stable Fe—O bond as compared to Ti—O bond. As a result, the rate performance is significantly enhanced exhibiting a reversible capacity of 73.7 mAh g^{-1} at 50 C for FTNO as compared to 37.9 mAh g^{-1} for its TNO counterpart. Besides, durable cycling is achieved by FTNO, which delivers a discharge capacity of 130.0 mAh g^{-1} after 6000 cycles at 10 C. Finally, the potential impact for practical application of FTNO anodes has been demonstrated by successfully constructing fast charging and stable $LiFePO_4$‖FTNO full cells.

1. Introduction

In order to meet the growing demand for fast charging lithium-ion batteries (LIBs) to enable the rapid development of portable devices and electric vehicles, various high-rate electrode materials have been recently developed.[1] The fast charging ability is dominated by the intrinsic crystalline structure of the involved materials to achieve optimal transport of Li^+ ions into the full interior of the electrode material.[2] In terms of anodes for LIBs, the intercalation-type materials are the most promising candidates for fast charging capability due to the suitable channels for Li^+ diffusion, as well as their long lifespan because of the stable crystal framework during repetitive cycling.[3–5] To date, Wadsley–Roth phase anodes are one of the most promising intercalation-type hosts for fast Li^+ transport because of the unique crystalline diffusion channels caused by the open structure exhibiting different types of octahedron-blocks separated by crystallographic shear planes.[6] Among them, mixed titanium niobium oxides, such as $Ti_2Nb_{10}O_{29}$, consisting of the 3×4 type of octahedron-blocks, can achieve a high theoretical capacity of 396 mAh g^{-1} (typically below 300 mAh g^{-1} in the voltage range of 3.0–1.0 V) based on the multiple reversible redox couples of Ti^{4+}/Ti^{3+}, Nb^{5+}/Nb^{4+}, and Nb^{4+}/Nb^{3+}.[7,8] Such high capacity exceeds that of graphite (372 mAh g^{-1}) and

J. Zheng, R. Xia, N. Yaqoob, P. Kaghazchi, J. E. t. Elshof, M. Huijben
University of Twente
MESA+ Institute for Nanotechnology
P. O. Box 217, Enschede 7500AE, The Netherlands
E-mail: m.huijben@utwente.nl
C. Sun, K. Zhao
State Key Laboratory of Advanced Technology for
Materials Synthesis and Processing
International School of Materials Science and Engineering
Wuhan University of Technology
Wuhan 430070, P. R. China
E-mail: kangning.zhao@epfl.ch

The ORCID identification number(s) for the author(s) of this article can be found under https://doi.org/10.1002/smll.202301967.

C. Sun
NRC (Nanostructure Research Centre)
Wuhan University of Technology
Wuhan 430070, P. R. China
N. Yaqoob, P. Kaghazchi
Forschungszentrum Jülich GmbH
Institute of Energy and Climate Research
Materials Synthesis and Processing (IEK-1)
52425 Jülich, Germany
Q. Qiu, Y. Li
Department of Chemical and Metallurgical Engineering
Aalto University
Kemistintie 1, Aalto FI-00076, Finland
L. Zhong, K. Zhao
Institute of Chemical Sciences and Engineering
Ecole Polytechnique Federale de Lausanne
Sion 1951, Switzerland

$Li_4Ti_5O_{12}$ (175 mAh g^{-1}), which have been the most common intercalation-type anodes in the past decades.[9–11] Furthermore, the suitable redox potential of titanium niobium oxides (≈1–2 V versus Li) avoids the decomposition of electrolyte and possible lithium plating on the electrode.[12]

So far, constructing nanostructures and nanohybrids by combining active electrode materials with conductive components has been widely utilized to enhance the fast charging ability as the diffusion length is dramatically reduced and the electronic conductivity is greatly enhanced.[13,14] However, these two strategies are inevitably accompanied by reduction of the tap density of the electrodes, which is attributed to the intrinsic low volumetric density of carbon as well as the high surface energy of nanomaterials. As a result, it will lead to insufficient volumetric capacities of the electrodes for most commercial applications. Furthermore, synthesis routes for production of nanostructures often involve multiple steps, which can be costly, time consuming, and hard to be achieved on the industrial scale.[15] Interestingly, it has been demonstrated that the high-rate ability can be achieved in specific bulk compounds with appropriate host framework, while a high volumetric capacity can be realized in such bulk electrodes due to the efficient packing of micro-sized active materials.[3–5] Therefore, micro-sized Wadsley–Roth phase titanium niobium oxides obtained by simple synthesis routes, such as solid-state reaction, have been proposed as promising high-rate electrodes for LIBs.[7,8,16]

In recent years, various strategies have been suggested to further improve the overall performance of micro-sized Wadsley–Roth phase titanium niobium oxides.[17] Considering the intrinsic low electronic conductivity of titanium niobium oxides, which is attributed to the empty 3d/4d orbitals in the *d* band of Ti/Nb,[18] creating oxygen vacancies and cation substitution have been demonstrated to successfully enhance the intrinsic electronic conductivity.[19–22] On the other hand, Wu et al. reported that the partial substitution of Nb^{5+} in $Ti_2Nb_{10}O_{29}$ by Ti^{4+} and W^{6+} reduces the crystallinity and induces an amorphous phase in which Li$^+$ diffusion becomes isotropic resulting in enhanced ionic transport.[23] Furthermore, Lv et al. indicated that the cation-mixing effect in the Wadsley–Roth phase is favorable for Li$^+$ diffusion and narrows the bandgap of the compound.[24] Lately, entropy tuning has received considerable interest due to the favorable entropy-dominated phase-stabilization and ionic conductivity boosting effects.[25–27] To date, it has only been applied in limited materials and the understanding of its function is still limited. Recently, Voskanyan et al.[28] reported that the entropy-stabilized Wadsley–Roth shear phases with more ordered structure would be stable upon electrochemical lithium (de-)insertion without phase transition, while more disordered structures would compromise the stability of the active material. Thus, suitable entropy tuning in entropy-stabilized Wadsley–Roth Shear Phases remains challenging and knowledge about its effect on crystal structure and lithium storage is still limited.

Here, entropy tuning by iron substitution in Wadsley–Roth phase titanium niobium oxides (molar ratio of Fe:Ti:Nb = 0.4:1.6:10, denoted as FTNO) has been demonstrated to enable fast and durable lithium storage performance. By increasing the entropy, the required annealing temperature to obtain phase-pure Wadsley–Roth FTNO was reduced to 1000 °C (denoted as FTNO-1000), at which its pristine counterpart, $Ti_2Nb_{10}O_{29}$ (denoted as TNO), fails to form the pure Wadsley–Roth phase, as a higher temperature (e.g., 1100 °C) is required. It has been reported that Li$^+$ diffusion is highly anisotropic in Wadsley–Roth phase titanium niobium oxides with activation energy barriers of ≈0.1–0.2 eV along the channels and ≈0.7–1.0 eV across the octahedron blocks.[29] Benefiting from the lower sintering temperature, FTNO-1000 shows a reduced grain size along the lithium diffusion favorable channels to enable the fast lithium ion diffusion kinetics as revealed by the kinetics analysis. More importantly, by investigating the structural evolution during the charge/discharge process via in situ X-ray diffraction (XRD), it is found that during (de)lithiation the lattice variation along the direction across the octahedron blocks, especially along *a*–axis, is reduced from ≈0.8% to ≈0.4% in FTNO as compared to TNO due to the more stable Fe−O bonds compared with Ti−O bonds as revealed by density functional theory (DFT) calculations. It suggests that the lithium intercalation channel in Wadsley–Roth phase is stabilized by tuning the entropy. As a result, FTNO-1000 exhibits an improved rate ability (specific capacity of 73.7 mAh g^{-1} at 50 C, while 1 C provides 395 mA g^{-1}) as compared to its 1100 °C counterparts (TNO-1100 and FTNO-1100). In addition, FTNO-1000 demonstrates an enhanced cycling durability (reversible capacity of 130.0 mAh g^{-1} after 6000 cycles at 10 C) as compared to pristine TNO. Furthermore, the practical full cell based on LiFePO$_4$/FTNO at a high areal capacity of 2 mAh cm^{-2} shows stable cyclability over 200 cycles at 5 C, demonstrating its potential application in the fast charging lithium ion battery.
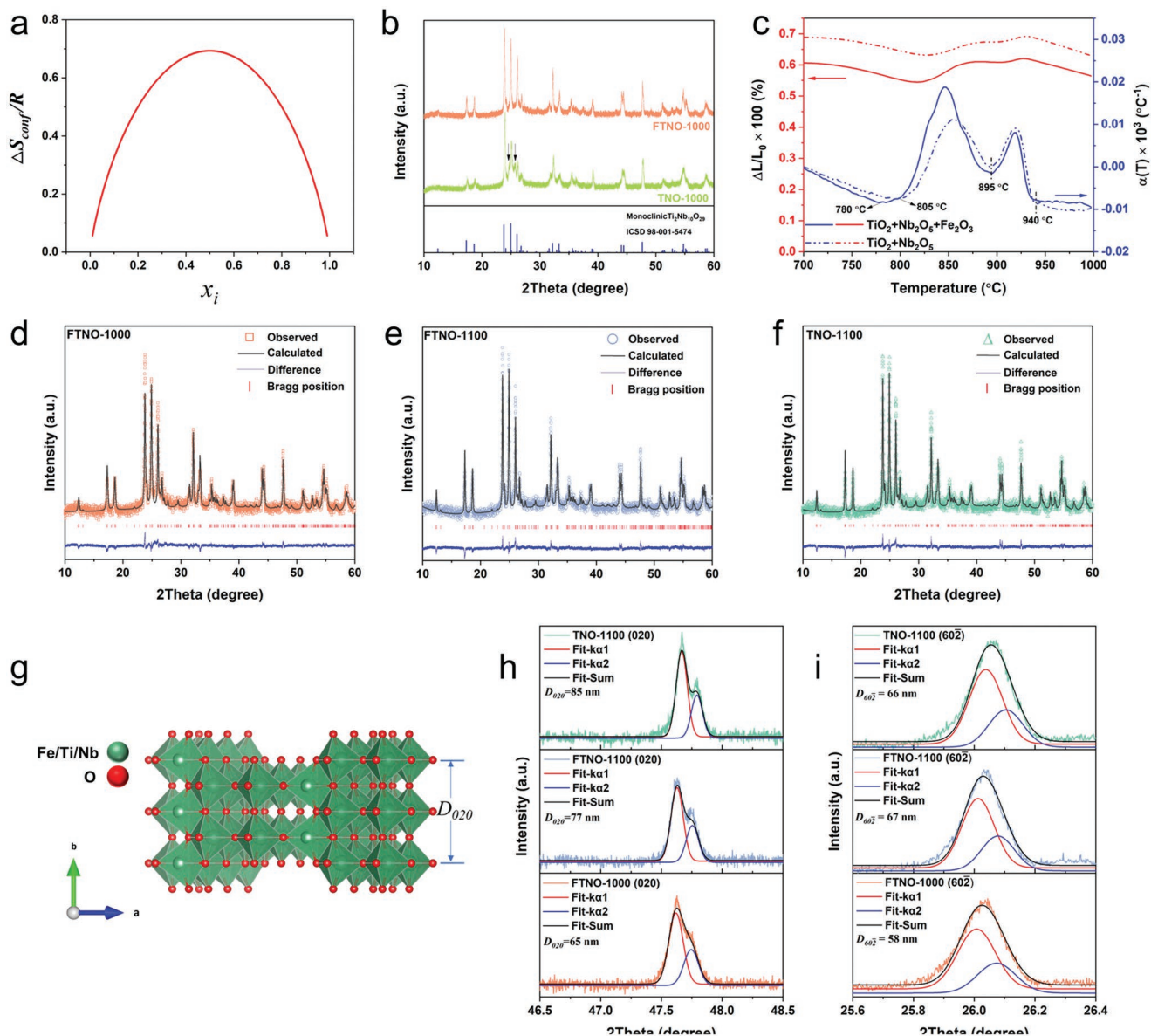
2. Results and Discussions

2.1. Structural Characterization

To understand the effect of iron substitution on entropy tuning, the configurational entropy (S_{config}) of the system is calculated by the equation below:[30,31]

$$S_{config} = -R\left[\left(\sum_{i=1}^{N} x_i \ln x_i\right)_{cation-site} + \left(\sum_{j=1}^{M} x_j \ln x_j\right)_{anion-site}\right] \quad (1)$$

in which x_i and x_j represent the mole fraction of elements present in the cation and anion sites, respectively. N or M indicates the number of components in the specific sites, while R is the universal gas constant. In our case, the mole ratios of Fe and Ti in original Ti sites are assumed as x_i and x_j, respectively. Thus, the (S_{config}/R)-x_i curve can be plotted to predict the entropy changing trend in the FTNO system (**Figure 1**a). When 20% of Ti is replaced by Fe, the S_{config}/R is calculated to be 0.5, suggesting the increase in the entropy in the system. Wadsley–Roth Ti-Nb-O compounds possess positive enthalpies of formation ($\Delta H_{f,ox}$) from parent binary oxides, implying that they are entropy-stabilized.[28] To obtain the entropy-stabilized Wadsley–Roth phase, the Gibbs free energy of formation ($\Delta G_{f,ox}$) should be negative in the following equation:

$$\Delta G_{f,ox} = \Delta H_{f,ox} - T\Delta S_{f,ox} \{at\ T(K)\} \quad (2)$$

**ADVANCED
SCIENCE NEWS**

www.advancedsciencenews.com

NANO · MICRO
small
www.small-journal.com

Figure 1. a) The plotted (S_{config}/R)–x_i curve from Equation (1); b) XRD patterns of TNO-1000 and FTNO-1000 powders; c) thermal expansion behavior of $TiO_2+Nb_2O_5$ and $Fe_2O_3+TiO_2+Nb_2O_5$ mixtures at the corresponding upper range from 700 to 1000 °C; Rietveld refinement of the XRD patterns of d) FTNO-1000, e) FTNO-1100, and f) TNO-1100; g) crystal structure of monoclinic FTNO and TNO phases along the c–axis; observed patterns and the corresponding fitted Kα1 and Kα2 curves of h) (020) peaks and i) (60$\bar{2}$) peaks of FTNO-1000, FTNO-1100, and TNO-1100.

where $\Delta H_{f,ox}$ is assumed invariant as the Nb content is unchanged in FTNO. Furthermore, $\Delta S_{f,ox}$ can be approximated as being S_{config} as the binary oxides are ordered. Thus, increasing entropy in the FTNO compounds is expected to decrease the required temperature to achieve the entropy-stabilized FTNO phase.

The crystal structure of the entropy tuned Wadsley–Roth phase FTNO is studied by XRD. As shown in Figure 1b, the major peaks of the iron-free titanium niobium oxide phase obtained at 1000 °C (denoted as TNO-1000) correspond to the monoclinic phase $Ti_2Nb_{10}O_{29}$, although two distinct peaks at ≈24.7° and ≈25.8° (marked with arrows) suggest the presence of impurity phases. These impurity peaks are most likely the

(004) and (60$\bar{2}$) peaks of $Nb_{12}O_{29}$ (space group A2/m), and can be attributed to the incomplete reaction between the TiO_2 and Nb_2O_5 starting powders, see Experimental Section. When 20 mol% of Ti^{4+} is substituted by Fe^{3+}, all the diffraction peaks of FTNO-1000 can be completely attributed to the monoclinic phase without any impurities. To further confirm the importance of entropy tuning, two other powders with ratio of "Fe:Nb = 1:11" and "Fe:Ti:Nb = 0.2:1.8:10," which are noted as FNO and FTNO0.2, were synthesized. For fair comparison, the same annealing procedure as $Fe_{0.4}Ti_{1.6}Nb_{10}O_{28.8}$ (1000 °C for 20 h) was applied. As shown in Figure S1a,b, Supporting Information, the XRD pattern of FNO presents the same impurity phase as TNO-1000. Furthermore, compared to TNO-1000, FTNO0.2

ADVANCED
SCIENCE NEWS
www.advancedsciencenews.com

NANO · MICRO
small
www.small-journal.com

shows a decreased intensity of the impurity peak (Figure S1c, Supporting Information). When the Fe ratio is even further increased (Figure S1d, Supporting Information, FTNO-1000), the impurity peaks are gone. Based on the above analysis, the importance of tuning entropy by Fe substitution in the FTNO system to obtain the Wadsley–Roth phase-pure powder at lower temperatures is proven.

To confirm the effect of Fe^{3+} substitution on boosting the solid-state reaction process, dilatometry (DIL) measurements were performed to measure the thermal expansion behavior of the mixtures of TiO_2-Nb_2O_5 and Fe_2O_3-TiO_2-Nb_2O_5, from room temperature up to 1000 °C with a constant heating rate of 5 °C min^{-1}. Two parameters are used to investigate the thermal expansion behavior: the linear thermal expansion ($\Delta L/L_0$) and linear thermal expansion coefficient ($\alpha(T)$), which can be defined by the following equations, respectively:

$$\frac{\Delta L}{L_0} = \frac{L_T - L_0}{L_0} \tag{3}$$

$$\alpha(T) = \frac{1}{L_0}\left(\frac{dL}{dT}\right)_p \tag{4}$$

in which L_0 represents the original length of the measured sample and L_T is the length of the sintered specimens at a specific temperature point T. $\alpha(T)$ indicates the length variation rate per degree of temperature. As depicted in Figure S2, Supporting Information, both mixtures exhibit shrinkage behavior below 100 °C owing to the evaporation of absorbed water. Subsequently, both mixtures show the same thermal expansion behavior up to 700 °C, above which a difference in $\alpha(T)$ with temperature can be observed. For the Fe_2O_3-TiO_2-Nb_2O_5 system, $\alpha(T)$ gradually decreases until 780 °C, after which a sudden increase can be observed, reaching a maximum at 845 °C. The latter behavior might be attributed to the formation of an intermediate Fe-Ti-Nb-O phase. The TiO_2-Nb_2O_5 mixture shows a similar trend, although $\alpha(T)$ starts increasing above 805 °C with a maximum at 857 °C. Besides, $\alpha(T)$ of the TiO_2-Nb_2O_5 mixture is always smaller than that of the Fe_2O_3-TiO_2-Nb_2O_5 system. Both these results indicate that the formation of an intermediate Ti-Nb-O phase, that is, $TiNb_2O_7$,[28] is less favorable in the TiO_2-Nb_2O_5 mixture. Both mixtures exhibit similar expansion behavior between 895 and 940 °C, which agrees well with the temperature range for the transition from T-Nb_2O_5 to H-Nb_2O_5.[32] Thus, it is reasonable to conclude that the observed expansion behavior relates to a phase transition from the intermediate phase to the final monoclinic phase. Based on these insights, we can conclude that with the increase of entropy, lower calcination temperature is required to obtain the complete pure entropy-stabilized Wadsley–Roth phase.

As comparison, TNO-1100 and FTNO-1100 were both synthesized at 1100 °C and their corresponding XRD patterns, together with that of FTNO-1000, are further analyzed through Rietveld refinement. As shown in Figure 1d–f, these three samples show prominent and sharp diffraction peaks, all of which can be indexed to the Wadsley–Roth phase with monoclinic A2/m space group. The refined lattice parameters of FTNO-1000, FTNO-1100, and TNO-1100 are summarized in

Table S1, Supporting Information. It can be observed that both FTNO samples have larger lattice values than TNO-1100, which can be attributed to the larger ionic size of Fe^{3+} (0.645 Å) as compared to Ti^{4+} (0.605 Å).[33] The larger unit cell volume of FTNO could also be beneficial for the Li^+ diffusivity along the active sites as the diffusion channels might be widened.[20] Furthermore, the grain sizes of FTNO-1000, and its 1100 °C counterparts, FTNO-1100 and TNO-1100, are determined by applying the Scherrer equation:[34]

$$D_{hkl} = \frac{K\lambda}{\beta\cos\theta} \tag{5}$$

where D_{hkl} is the grain size perpendicular to the *(hkl)* crystal planes, K is the shape factor, λ is the X-ray wavelength, β represents the full width of the peak at half maximum (FWHM) and θ is the diffraction angle. To confirm the validity of applying Scherrer equation to determine the grain size, the effects of size and strain on broadening of the Bragg peaks are separated based on Williamson-Hall methods (Figure S3, Supporting Information).[35] The results suggest that the effect of strain on broadening of XRD peaks of FTNO and TNO is much less than that of grain size. Figure 1g shows a schematic of the crystal structure of monoclinic FTNO in which the aforementioned Li^+ diffusion channel with the lowest energy barrier is directed along the *b* direction and thus perpendicular to the (020) plane. Based on this consideration, the (020) diffraction peak was selected for calculation of D_{020}, which represents the length of the diffusion channel. Kα1 peaks were extracted from the raw diffraction patterns and fitted by the Gaussian method, as shown in Figure 1h. The obtained FWHM of FTNO-1000, FTNO-1100, and TNO-1100 are summarized in Table S2, Supporting Information. The FTNO-1000 samples exhibit a broader (020) diffraction peak caused by reduced grain size. The D_{020} of FTNO-1000 is determined to be ≈65 nm, which is smaller than that of its 1100 °C counterpart (e.g., ≈85 nm for TNO), confirming the effect of shortening the Li^+ diffusion channel length. Additionally, the (60$\bar{2}$) peaks were also selected to determine the grain size along the *a/c* direction. The obtained FWHM values are summarized in Table S2, Supporting Information, and the calculated grain sizes are shown in Figure 1i. The smaller grain size of FTNO-1000 along *a/c* direction suggests that the lower annealing temperature will not only shorten the diffusion channel length but also lead to the smaller crystalline domains and thereby introduce more grain boundaries, which will boost the Li^+ transfer as well.[36,37]

In order to get further insight into the bonding characteristics of the specific crystal structures, Raman spectroscopy was utilized and the patterns are shown in Figure S4, Supporting Information. The stretching vibration of NbO_6 and TiO_6 octahedra in both FTNO and TNO samples give rise to two groups of characteristic peaks at 896/1000 cm^{-1} and 854/645 cm^{-1}, respectively.[38] Besides, the bending vibration of O−Ti−O/O−Nb−O bridging bonds leads to the evident peaks at 273 cm^{-1} for all these samples. The substitution of Ti^{4+} with Fe^{3+} does not change the Raman spectrum of FTNO, as the Raman peaks for the bending vibration of O−Fe−O bridging bonds and the stretching vibration of FeO_6 octahedra are located at similar positions as the Raman peaks originating

**ADVANCED
SCIENCE NEWS**

www.advancedsciencenews.com

**NANO · MICRO
small**

www.small-journal.com

from O−Ti−O/O−Nb−O bonds and TiO_6 octahedra, respectively.[39] In addition, X-ray photoelectron spectroscopy (XPS) was employed to study the elemental chemical nature of a FTNO-1000 sample (Figure S5, Supporting Information). The Ti 2p spectrum exhibits two broad peaks at 458.9 and 464.7 eV, confirming the typical Ti^{4+} state in the FTNO-1000 sample.[40] The broad and weak peaks of Ti 2p spectra should be attributed to the low atomic concentration of Ti^{4+}. In addition, as the XPS technique can only focus on the surface and near-surface areas, Fe^{3+} fails to arise any signal due to the bulk morphology of the powder and the even lower concentration of iron present. However, the valence of iron in FTNO samples is confirmed by electrochemical analysis, as discussed in the following section. Moreover, the Nb 3d spectrum displays two sharp peaks at 207.3 and 210.0 eV, corresponding to the Nb^{5+} oxidation state in FTNO-1000.
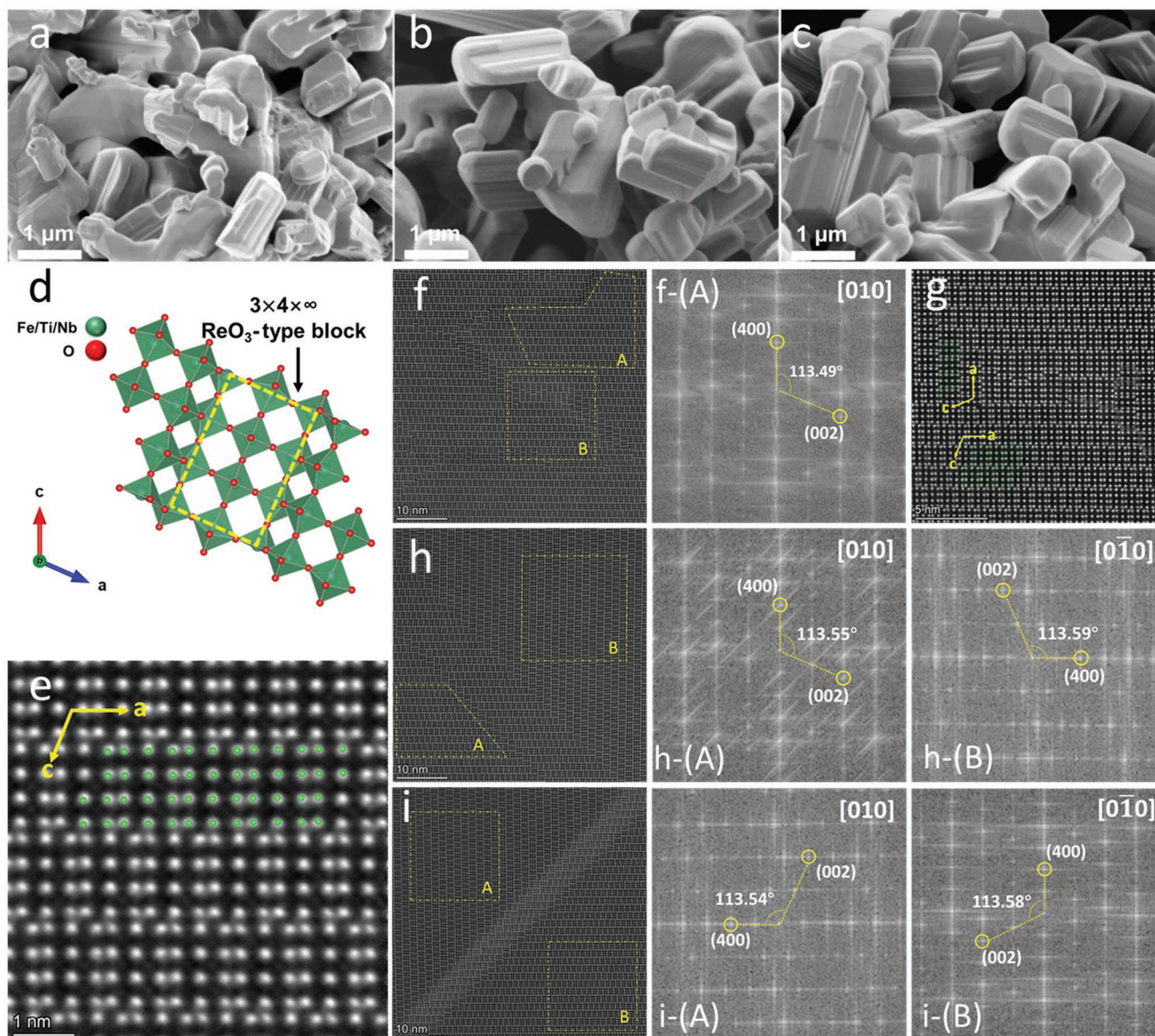
The size and morphology of FTNO-1000, FTNO-1100, and TNO-1100 powders were characterized by scanning electron microscopy (SEM). As shown in **Figure 2**a–c, all of these three samples possess an irregular shape based on agglomerated bulk particles, of which sizes are typically larger than 1 µm. Elemental energy-dispersive X-ray spectroscopy (EDX) mapping of FTNO-1000 (Figure S6, Supporting Information) shows the homogenous distribution of not only the Ti, Nb, and O elements but also the Fe element, thus indicating the homogenous substitution of Ti^{4+} by Fe^{3+} in the obtained Wadsley–Roth phase. X-ray fluorescence (XRF) analysis confirmed the atomic ratio of Fe:Ti:Nb, which is summarized in Table S3, Supporting Information. The atomic ratios of Fe:Ti:Nb for FTNO-1000 and FTNO-1100 are determined to be 1:3.65:24.33 and 1:3.85:25.72, respectively, both of which are close to the theoretical atomic ratio of 1:4:25. In addition, the Brunauer–Emmett–Teller method (BET) was conducted to investigate the specific surface area of the FTNO and TNO samples. As shown in Figure S7, Supporting Information, all samples exhibit similar nitrogen adsorption-desorption isotherms owing to the similar micro-sized bulk morphologies. Based on the nitrogen adsorption behavior, the BET surface areas of FTNO-1000, FTNO-1100, and TNO-1100 have been calculated to be 1.2176 ± 0.0023, 1.1048 ± 0.0022, and 1.0053 ± 0.0042 $m^2 g^{-1}$, respectively, in good agreement with the measured grain size variation.

Furthermore, high angle annular dark field scanning transmission electron microscopy (HAADF-STEM) was applied to characterize the detailed crystal structure of the particles. Figure 2d presents the schematic diagram of FTNO, or TNO, crystal structure along the *b*–axis, in which the typical $3 \times 4 \times \infty$ ReO_3-type shear blocks are marked. The cation distribution in the *a*–*c* plane of such typical ReO_3-type shear structure was previously revealed by neutron diffraction.[41] It indicated a preferred occupancy of Nb^{5+} in the center sites of the block with a more likely distribution of the lower charged cation in the edge and corner sites. To characterize the periodic atomic arrangement in the *a*–*c* plane of all samples, the focused ion beam (FIB) technique was applied to extract specimens perpendicularly to the *b*–axis (Figure S8, Supporting Information). Figure 2e displays the local atomic arrangement in the *a*–*c* plane of individual grain in FTNO-1000 and it corresponds to the grain zone A in Figure 2f. The typical $3 \times 4 \times \infty$ ReO_3-type shear blocks are clearly identified and they exhibit exactly the

same atomic regularity as the crystal structure model (marked with green dots), confirming the identical cation distribution type in the *a*–*c* plane of FTNO-1000 as the conventional Wadsley–Roth phase $Ti_2Nb_{10}O_{29}$. Furthermore, Fast Fourier Transform (FFT) analysis is performed on zone A in Figure 2f. Figure 2f-A clearly reveals (400) and (002) miller planes on the [010] zone axis and the angle between them is 113.49°, confirming the monoclinic structure of FTNO-1000. Additionally, the grain boundaries of FTNO-1000, corresponding to the zone B of Figure 2f, are shown in Figure 2g. It can be observed that the blocks are ≈90° rotated in-plane with respect to the adjacent grain and they are mirror symmetrical around (400)-plane. Apart from that, the lattice reconstructions and cation vacancies are mainly present in the grain boundaries, while both FTNO-1100 and TNO-1100 exhibit the integral blocks (Figure S9, Supporting Information). This can probably be attributed to the lower sintering temperature and is expected to boost the Li^+ transfer kinetics along the grain boundaries. As for FTNO-1100 and TNO-1100, the atomic arrangement within individual grains (zone A or B in Figure 2h,i, respectively) displays the typical $3 \times 4 \times \infty$ ReO_3-type shear blocks as well. Combined with the related FFT images (Figure 2h-A/B and i-A/B), which reveal the (400) and (002) planes with ≈113.5° angle with respect to each other, it is further confirmed that the monoclinic FTNO-1000/1100 and TNO-1100 with typical Wadsley–Roth phase are successfully obtained. Moreover, as revealed in the FFT images, the adjacent grains (zone A and B) in both FTNO-1100 and TNO-1100 also show the 90° in-plane rotation behavior and mirror symmetry. Given the fact that FTNO-1000 possesses the same atomic arrangement and mirror symmetrical adjacent grains as FTNO-1100 and TNO-1100, it can be concluded that with the increase of entropy through iron substitution, FTNO-1000 with a shortened Li^+ diffusion pathway is able to maintain the typical character of ReO_3-type blocks in the *a*–*c* plane.
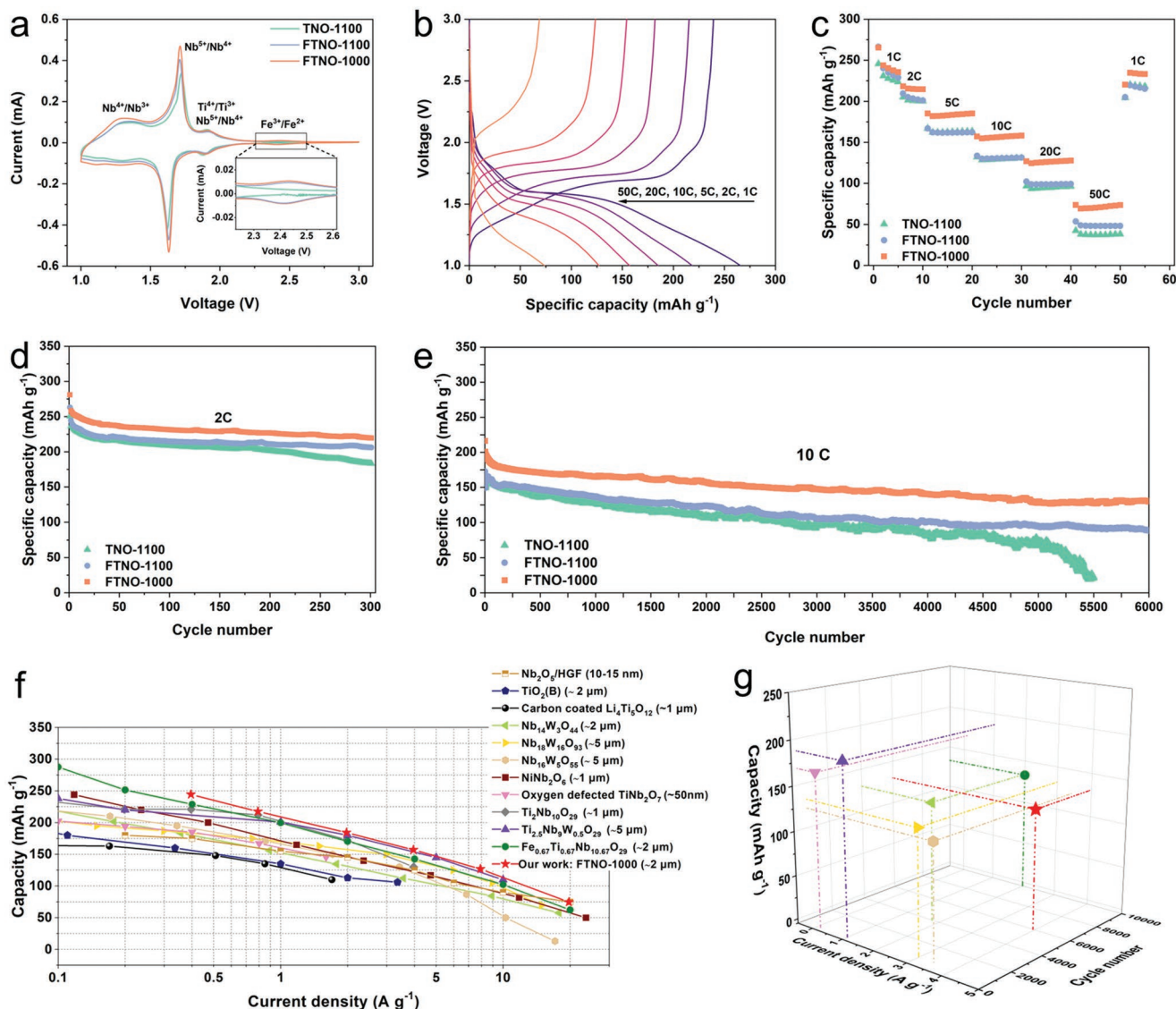
2.2. Electrochemical Characterization

In order to study the influence of the entropy tuning on the electrochemical lithium storage performance, various electrochemical techniques were applied to half cells consisting of an FTNO/TNO working electrode and a lithium metal counter electrode. Cyclic voltammetry (CV) was conducted to investigate the basic redox behavior of FTNO-1000, FTNO-1100, and TNO-1100 electrodes. As shown in **Figure 3**a, both FTNO-1000 and FTNO-1100 show a weak and broad bump at around 2.41 V, which is assigned to the Fe^{3+}/Fe^{2+} redox couple and indicates the Fe^{3+} state in the pristine FTNO samples.[42,43] Except for this bump, all three electrodes exhibit a similar redox process from 1.0 to 2.25 V, in which the first pair of redox peaks located at ≈1.9 V corresponds to the redox couples of Ti^{4+}/Ti^{3+} and Nb^{5+}/Nb^{4+}.[44] The second pair of sharp peaks at ≈1.65 V originates from the Nb^{5+}/Nb^{4+} redox process.[38,45,46] A pair of broad bumps from ≈1.0–1.4 V should correspond to the Nb^{4+}/Nb^{3+} redox couple.[38] The galvanostatic charge–discharging technique was applied to investigate the rate performance of the electrodes. Figure 3b shows the charge–discharged profiles of the initial cycle of FTNO-1000 electrode under different C-rates. Typically, the profiles at 1 C exhibit three evident lithiation/delithiation

**ADVANCED
SCIENCE NEWS**

www.advancedsciencenews.com

**NANO · MICRO
small**

www.small-journal.com

Figure 2. SEM images of a) FTNO-1000; b) FTNO-1100, and c) TNO-1100. d) Schematic diagram of the FTNO, or TNO, crystal structure along the *b*–axis. e,f) HAADF-STEM images of FTNO-1000 and the corresponding FFT images. g) HAADF-STEM images of FTNO-1000 with higher magnification selected from zone B in (f). HAADF-STEM and FFT images of h) FTNO-1100 and i) TNO-1100.

stages located at $\approx$3–1.7 V, $\approx$1.7–1.4 V, and $\approx$1.4–1.0 V, respectively, which are in good agreement with the observed redox processes measured by CV. With the incremental increase of the C-rate from 1 C to 50 C, the FTNO-1000 electrode possesses a high coulombic efficiency at each rate and delivers discharge capacities of 263.7, 217.5, 184.3 157.1, 126.9, and 73.7 mAh g^{-1}. In comparison, the 1100 °C counterparts, FTNO-1100 and TNO-1100, fail to achieve comparable rate performances. As shown in Figure 3c, the three electrodes display similar capacities at a relatively low C-rate. However, compared to FTNO-1000 electrodes, the capacities of FTNO-1100 and TNO-1100 drop significantly when the rate increases gradually from 2 to 50 C, delivering only 48.8 and 37.9 mAh g^{-1} at 50 C. The superior rate ability of FTNO-1000 is prominent among the previously reported micro-sized TiO$_2$(B),[47] Li$_4$Ti$_5$O$_{12}$,[48] Ti-Nb-O system (Ti$_2$Nb$_{10}$O$_{29}$,[7] Ti$_{2.5}$Nb$_9$W$_{0.5}$O$_{29}$[23] and Fe$_{0.67}$Ti$_{0.67}$Nb$_{10.67}$O$_{29}$[24]) and other Metal-Nb-O system (Nb$_{16}$W$_5$O$_{55}$/Nb$_{18}$W$_{16}$O$_{93}$,[3] Nb$_{14}$W$_3$O$_{44}$[4] and NiNb$_2$O$_6$[5]). Moreover, it is also comparable to nanocomposite of Nb$_2$O$_5$ with holy graphene (Nb$_2$O$_5$/HGF) and outperforms some nano-sized Ti-Nb-O (e.g., oxygen-defected TiNb$_2$O$_7$ nanoparticles).[49,50] Besides, FTNO-1000 shows a competitive rate performance within voltage range of 3.0–1.0 V as compared to some other Nb-based anodes which were tested with the cut-off voltage of 0.01 V (Table S4, Supporting Information).[51,52] Additionally, the volumetric capacity, which is important for practical application, is determined for FTNO-1000 based on the measured tap density (1.7 g cm^{-3}) and the corresponding results are

**ADVANCED
SCIENCE NEWS**

www.advancedsciencenews.com

**NANO · MICRO
small**

www.small-journal.com

Figure 3. a) CV curves of FTNO-1000, FTNO-1100, and TNO-1100 electrodes at sweep rate of 0.1 mV s^{-1}; b) initial cycle charge–discharge curves of FTNO-1000 from 1 to 50 C, where 1 C = 395 mAh g^{-1}; c) rate performance of FTNO-1000, FTNO-1100, and TNO-1100; d,e) long-term cycling performance of FTNO-1000, FTNO-1100, and TNO-1100 under d) 2 C and e) 10 C. f) Rate and g) cycling performance comparison of FTNO-1000 with other Ti-based and Nb-based oxides, of which the voltage ranges are 3.0–1.0 V.

summarized in Table S5, Supporting Information. The FTNO-1000 exhibits comparable volumetric capacity to the micro-sized Nb-W-O oxides with relatively high tap density and outperforms the nano-sized Nb$_2$O$_{5-x}$ at lower current density.[3,53] Some other recently developed anodes with high tap density and volumetric capacity are also included for comparison.[54–57]

The superior rate performance of FTNO-1000 is expected to be caused by the shortened Li$^+$ diffusion channel length as well as the smaller grain size, of which the effect on the specific Li$^+$ transfer kinetics within these three electrode materials will be discussed below. The long-term cycling stability of the electrodes was also investigated at 2 and 5 C. Initial 5 cycles are activation of the electrodes and calculation of the capacity retentions presented below are based on the discharge capacities at sixth cycle. Charge–discharged profiles of the first,

second, 50th, 100th, 200th, and 300th cycles at 2 C are depicted in Figure S10a–c, Supporting Information. The initial coulombic efficiencies of FTNO-1000, FTNO-1100, and TNO-1100 are calculated to be 90.4%, 93.0%, and 93.6% and remain stable over the full cycling process (Figure S10d, Supporting Information). However, TNO-1100 shows a more dramatic capacity degradation and a larger polarization of the voltage plateaus after 300 cycles as compared to FTNO electrodes. As shown in Figure 3d, FTNO-1000 and FTNO-1100 present a more stable cycling performance at 2 C after 300 cycles with a similar capacity retention of 87.1 and 87.5%, respectively, while the TNO-1100 shows a lower capacity retention of 79.3%. The enhanced cycling stability of FTNO-1000 and FTNO-1100 electrodes is also observed when cycling was performed under 10 C for 6000 cycles, as shown in Figure 3e. The FTNO-1000

ADVANCED
SCIENCE NEWS
www.advancedsciencenews.com

NANO · MICRO
small
www.small-journal.com

and FTNO-1100 electrodes can deliver discharge capacities of ≈ 130 and 89 mAh g^{-1} after 6000 cycles with capacity retentions of 66.1% and 56.3%. In comparison, TNO-1100 only delivers a reversible capacity of ≈ 21 mAh g^{-1} with the capacity retention of 13.5%. The cycling stability of FTNO-1000 is also competitive compared to the other micro-sized Wadsley–Roth phase oxides previously reported (Figure 3g).[3–5,23,24] These results indicate the positive effect of iron substitution on stabilizing the structure during extensive cycling. Given the fact that the structural stability of the host mainly depends on the lattice evolution behavior during the repetitive insertion/extraction of Li$^+$ ions, detailed in situ XRD analysis was conducted and will be discussed later.

2.3. Lithium-Ion Diffusion Mechanism

Aiming at clarifying the effect of a shortened Li$^+$ diffusion channel and a reduced grain size on the Li$^+$ transfer kinetics within the electrodes discussed above, CV analysis at various scan rates was conducted to study the Li$^+$ diffusion coefficient in these three electrode materials. **Figure 4**a–c presents the CV curves from 0.1 to 2.0 mV s^{-1}, of which the major oxidation and reduction peaks are marked as A and B, respectively. As the scan rates increase, these three electrodes exhibit a major peak shifting, which should be attributed to an increase in the ohmic resistance and the polarization (electrochemical polarization and concentration polarization). However, the degree of the shifting is obviously different for these three electrodes and will be discussed in depth later. To get insight into the lithium-ion diffusion kinetics of the three electrodes, peaks currents (I_p) of various CV curves at different scan rates (ν) are collected and the apparent Li$^+$ diffusion coefficient (D_{Li^+}) is obtained according to the Randles–Sevcik equation:[58]

$$I_p = 2.69 \times 10^5 An^{1.5} C D_{Li^+}^{0.5} \nu^{0.5} \tag{6}$$

where the A and n represent the electrode area and the charge transfer number, respectively, and C refers to the molar concentration of lithium-ions in the electrode. As shown in Figure 4d,e, the linear relationship between peak current and square root of the scan rate are present for both A and B peaks in these three electrodes. However, FTNO exhibits a steeper slope of the I_p–$\nu^{0.5}$ curves, which has a positive correlation with the D_{Li^+}, than FTNO-1100 and TNO-1100. Thus, the favorable Li$^+$ diffusion kinetics in the FTNO-1000 electrode is confirmed by the higher D_{Li^+} values for both cathodic and anodic processes, as shown in Figure 4f. Furthermore, to study the trend of the evolution of the overpotential and its corresponding limiting factors in the reaction rate and the diffusion process, a recently developed theoretical model was applied, which can be summarized by the following equation:[59]

$$i_0' = nFAk_0C = \frac{1}{\tau M} \tag{7}$$

$$i_l' = nFA\frac{D_{Li^+}}{\delta}C = \frac{1}{\tau N} \tag{8}$$

$$E_p = E_{eq} + \Delta E_{od} + \Delta E_t = E_{eq} - i_p R_0 + \frac{2}{f}\ln\left(\frac{-Mi_p + \sqrt{4 + M^2 i_p^2 - 4Ni_p^2}}{2 + 2Ni_p}\right) \tag{9}$$

In Equations (7) and (8), i_0' and i_l' are the exchange current and diffusion-limited current at maximum current, respectively. In particular, k_0 represents the reaction rate constant while D_{Li^+} refers to the diffusion coefficient. τ is the shape factor, which equals 1 in our analysis due to the fact that the morphology of the powder is micron-sized. To simplify Equations (7) and (8), M and N are defined as the elements which are related with i_0' and i_l'. In Equation (9), E_p and i_p refer to the voltage and the corresponding current at the current maximum. E_{eq} is the voltage at equilibrium state. ΔE_{od} refers to the ohmic potential drop which originated from the ohmic resistance (R_0). ΔE_t is the overpotential which is determined by the M and N, thus the reaction rate constant (k_0) and diffusion constant (D_{Li^+}). The total potential drop (ΔE) is composed of ΔE_{od} and ΔE_t. In order to prevent the merging of the major peaks with the adjacent bump under the high scan rates, the CV measurements of the electrodes were carried out at various scan rates from ≈ 0.2–0.6 mV s^{-1}, as shown in Figure S11, Supporting Information. By collecting a series of E_p-i_p points, the curves of ($\Delta E_{od} + \Delta E_t$)-$i_p$ can be fitted using Equation (9). The fitted components are summarized in Table S6, Supporting Information. As depicted in Figure 4g, the total potential drop of the FTNO-1000 electrode is always smaller than that of the FTNO-1100 and TNO-1100 electrodes. Besides, the first deviation of ΔE_t–i curves, as shown in Figure 4h, indicates that the FTNO-1000 electrode exhibits the least possibility of generating overpotential, especially at the low current range. In order to separate the effect of reaction rate and diffusion process on the generation of overpotential, the normalized i_0'/A and i_l'/A, which have a positive correlation with k_0 and D_{Li^+}, respectively, are summarized in Figure 4i. It is obvious that the FTNO-1000 electrode shows higher k_0 and D_{Li^+} values, indicating that the significantly enhanced Li$^+$ reaction and transfer kinetics in FTNO-1000 electrode contributes to the reduced overpotential, and thus the improved rate performance.

Furthermore, Electrochemical Impedance Spectroscopy (EIS) measurements were conducted to investigate the electronic conductivity within the electrodes in the charged state, as shown in Figure S12a, Supporting Information. As the redox potential of Fe^{3+}/Fe^{2+} is at ≈ 2.4 V, which is confirmed by CV analysis shown in Figure 3a, the open circuit voltage (OCV) of FTNO electrodes in the charged state is higher than that for a TNO-1100, thus causing the different potential of the charged state. An equivalent circuit (Figure S12b, Supporting Information) is used to fit the Nyquist plots of all three electrodes. The element R2 refers to the charge transfer resistance and corresponds to the first semicircle within the Nyquist plots,[60] for which the high frequency areas are zoomed in and, shown in Figure S12c,d, Supporting Information. The fitted R2 values for FTNO-1000, FTNO-1100, and TNO-1100 electrodes are 17.88, 23.02, and 21.18 Ω, respectively, indicating that the iron substitution would not affect the electronic conductivity of the electrodes significantly. This might be attributed to the half-full 3d orbitals of Fe^{3+}, in which the 3d electrons tend to be stable.[61]

As discussed above, FTNO electrodes present an enhanced cycling performance as compared to TNO-1100 electrodes,

**ADVANCED
SCIENCE NEWS**

www.advancedsciencenews.com
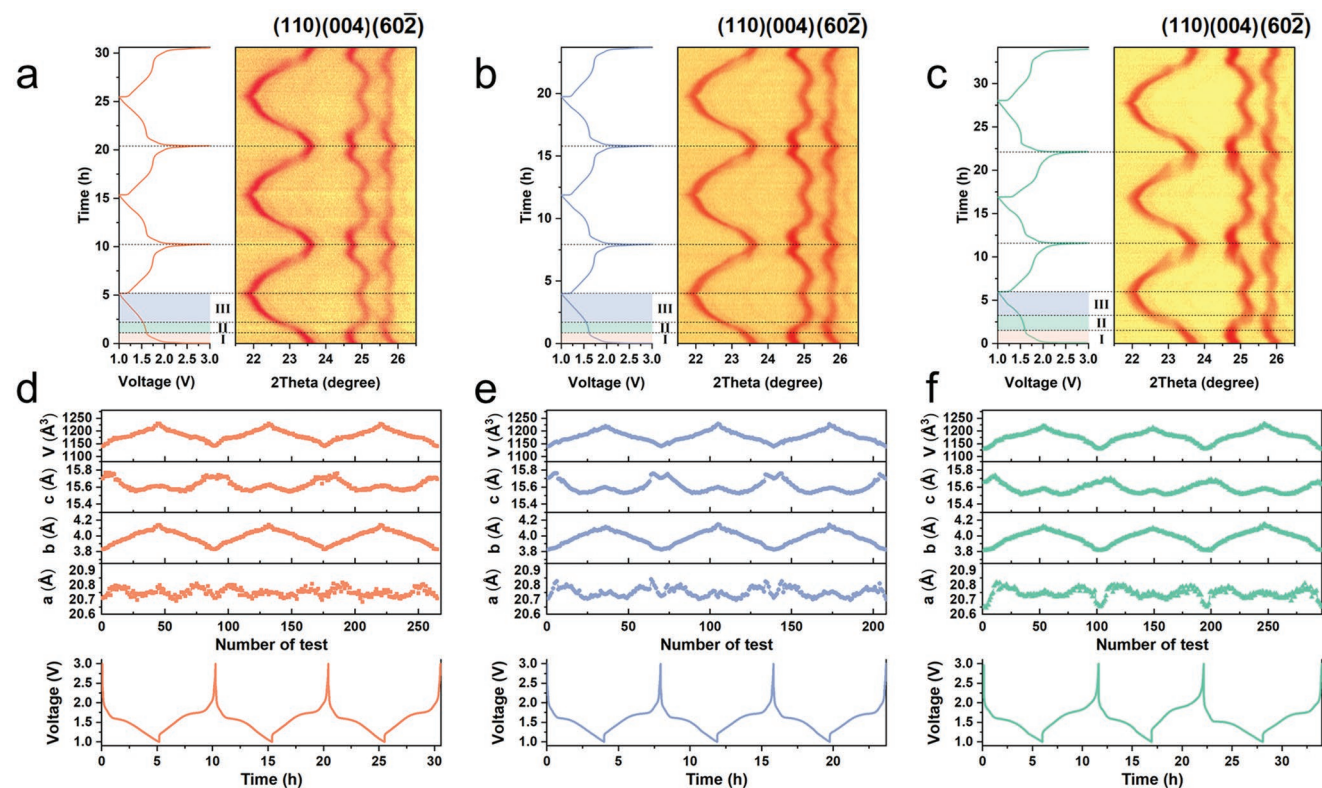
NANO · MICRO

small

www.small-journal.com
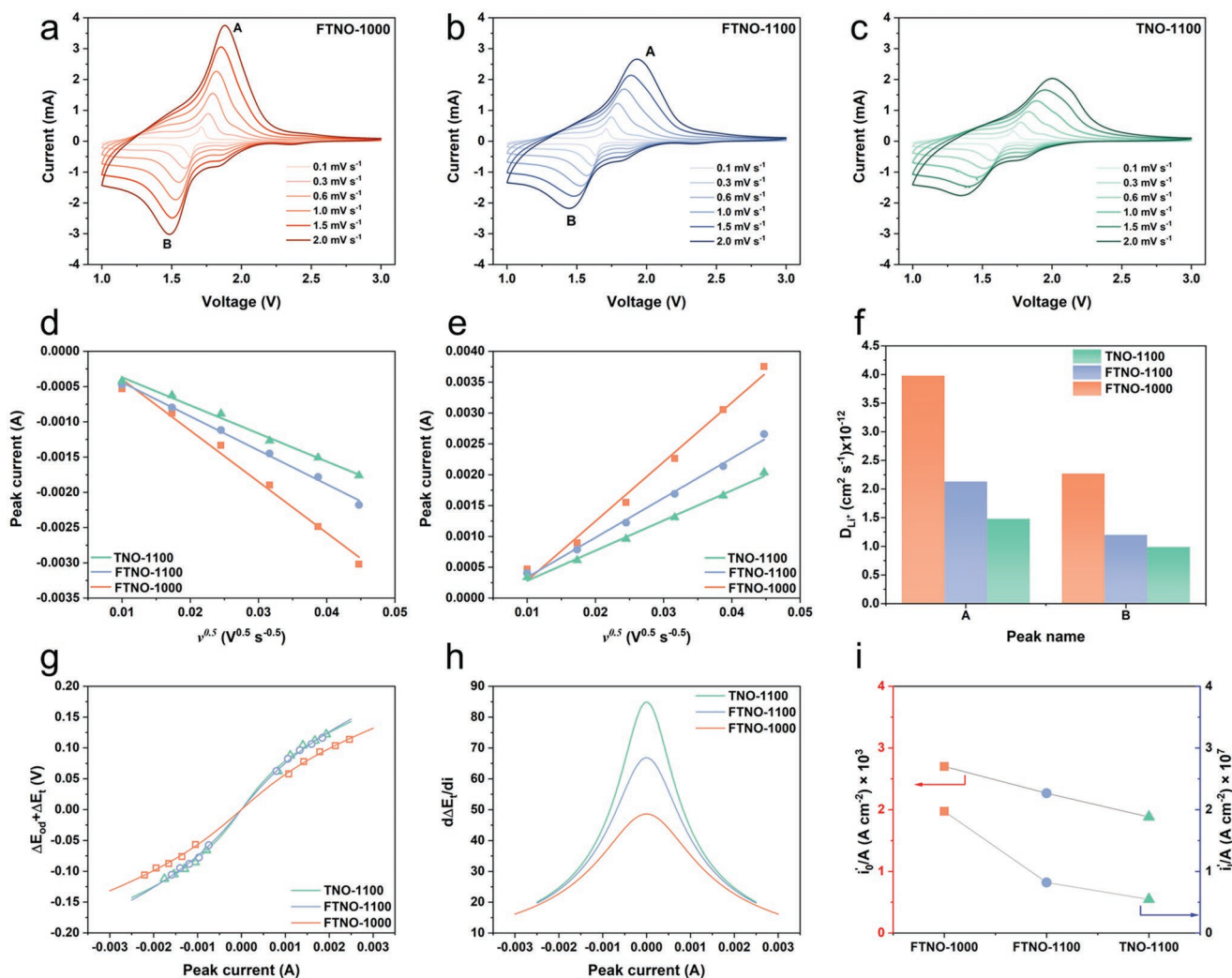
Figure 4. The CV curves of a) FTNO-1000, b) FTNO-1100, and c) TNO-1100 at different scan rates; linear relationship between the major d) reduction and e) oxidation peaks current and square root of scan rates; f) Li$^+$ diffusion coefficient of FTNO-1000, FTNO-1100 and TNO-1100 electrodes; g) the relationship between total potential drop ΔE ($\Delta E = \Delta E_{od} + \Delta E_t$) and peak current ($i_p$) and their fitted lines; h) the first deviation of ΔE_t–i_p curves; i) the normalized i_0' /A and i_l' /A of FTNO-1000 and FTNO-1100 and TNO-1100 electrodes.

which could be correlated with a different structural evolution of the active materials upon repeated lithiation/delithiation processes. Therefore, in situ XRD is utilized to investigate the structural variation of FTNO-1000, FTNO-1100, and TNO-1100 electrodes for the successive three cycles in the potential range of ≈1.0–3.0 V. As shown in Figure S13, Supporting Information, the overall 2D in situ XRD contour maps present the diffraction peaks which are all consistent with the XRD analysis (Figure 1d–f). In particular, the specific patterns in the 2θ range of ≈21.5–26.5° are extracted for discussion as it includes the three main peaks of (110), (004), and (60$\bar{2}$) which correspond to a–, b– and c–axis lattice information.

Thus, **Figure 5**a–c shows the selected in situ XRD contour maps and their corresponding charge–discharged curves of FTNO-1000, FTNO-1100, and TNO-1100 electrodes, respectively. For the first lithiation process of TNO-1100, the overall discharged curve can be divided into three stages. For stage I, ranging from ≈3.0–1.7 V, all three diffraction peaks move

continuously to lower angles without the appearance of new peaks, indicating a solid-state solution process. The subsequent stage II, ranging from ≈1.7–1.5 V, corresponds to the plateau area, in which the peak broadening and peak shifting between 23.25° and 22.5° are attributed to a two-phase transformation.[7] Actually, a similar two-phase transformation at the plateau region has been reported for the other Wadsley–Roth Phase titanium niobium oxides.[62,63] The final stage III, ranging from ≈1.5–1.0 V, is related to the second solid-solution process as all three diffraction peaks exhibit a continuous shift. The reversible peak shifting is observed for the delithiation process during subsequent charging, as well as the same trend for the following two cycles, which confirms the typical reversibility of the obtained TNO-1100 electrodes. The same trend of peak changing and high reversibility is observed for both FTNO-1000 and FTNO-1100 electrodes, confirming that the iron substitution will not change the original lithiation mechanism in the Wadsley–Roth phase Ti$_2$Nb$_{10}$O$_{29}$. By extraction from the original

**ADVANCED
SCIENCE NEWS**

www.advancedsciencenews.com

NANO · MICRO

small

www.small-journal.com

Figure 5. The selected in situ XRD contour map at ≈21.5–26.5° and the related charge–discharged curves of a) FTNO-1000, b) FTNO-1100, and c) TNO-1100; the unit cell lattice parameters evolution of d) FTNO-1000, e) FTNO-1100, and f) TNO-1100 with the corresponding charge–discharged process.

in situ profiles, the individual lattice parameter changes provide deeper insight into the lithiation mechanism. As shown in Figure 5d–f, all three electrodes present a coupled behavior of the a/c–axes and an independent expansion of the b–axis upon the lithiation process. For the subsequent delithiation, the contraction of the b–axis and the coupled change of the a/c–axes indicate the reversible lattice deformation along all directions. Such anisotropy in the lattice changes has also previously been reported and the underlying mechanism was revealed to be Li occupying various sites at different states and thus leading to distinct lattice changing behavior.[64,65] Furthermore, the lithiation-induced expansion rate (%) of the lattice parameters Δa, Δb, Δc, and ΔV for all electrodes are depicted in Figure S14, Supporting Information. Although the volume changes (ΔV) of FTNO-1000 and FTNO-1100 are ≈7.69 and 7.14%, which are close to that of TNO-1100 (≈8.0%), the changes for the specific lattice parameters within FTNO-1000, FTNO-1100, and TNO-1100 exhibit detailed disparity during the different stages. In particular, Δa for FTNO-1000 and FTNO-1100 at the end of stage I decrease from ≈0.8% to ≈0.4% as compared to TNO-1100. However, Δb and Δc remain to be similar during the full lithiation/delithiation process. These results suggest that iron substitution in the Wadsley–Roth phase Titanoniobate suppresses the expansion along the a-direction, especially at the low lithiation level (corresponding to stage I in Figure 5a–c), thus stabilizing the 3 × 4 octahedral blocks, which contain the Li+ diffusion channels.

2.4. Theoretical Modeling

In order to gain fundamental insight into the mechanism causing the suppression of the lattice expansion by iron substitution, DFT calculation was applied to model the lattice variation during the lithiation. The low lithiation level, at which the suppression effect is observed, is considered for FTNO and TNO in the modeling process. Considering the charge balancing mechanism, the Fe-substituted TNO model is set as $Fe_1Ti_1Nb_{10}O_{28.5}$, where the valence of Fe is 3+. Thus, the atomistic structures of bare and Fe-substituted titanoniobate without and with Li, namely $Ti_2Nb_{10}O_{29}$, $Li_1Ti_2Nb_{10}O_{29}$, $Fe_1Ti_1Nb_{10}O_{28.5}$, and $Li_1Fe_1Ti_1Nb_{10}O_{28.5}$, were determined by performing an extensive set of Coulomb energy and DFT calculations. Aiming to confirm the reduction sequence of different elements, the redox mechanism is studied first by computing the electron density of states (DOS) of $Ti_2Nb_{10}O_{29}$ with and without the Fe substitution as well as Li intercalation. Figure S15, Supporting Information shows that for both cases without and with iron substitution, after lithiation the bandgap becomes narrower indicating an increase in the electronic conductivity. For $Ti_2Nb_{10}O_{29}$, the low-lying unoccupied bands mainly consist of the 3d orbitals of Ti^{4+} showing that Ti cations would experience reduction with lithiation. This can also be observed in the calculated DOS for $Li_1Ti_2Nb_{10}O_{29}$ in comparison to that for $Ti_2Nb_{10}O_{29}$ indicating that some Ti 3d bands are occupied, which means that the $Ti^{4+} \rightarrow Ti^{3+}$ reduction takes place with lithiation.

**ADVANCED
SCIENCE NEWS**

www.advancedsciencenews.com

NANO · MICRO

small

www.small-journal.com

This has also been confirmed by the computed number of unpaired electrons and oxidation states of elements in Table S7, Supporting Information. These results show that the reduction of Ti^{4+} happens before Nb^{5+} reduction. In the case of Fe substitution without Li (Figure S15c, Supporting Information), the presence of occupied spin-down Fe 3d orbitals confirms that Fe^{3+} is in low spin state. The low-lying unoccupied bands stem mainly from the Fe 3d orbitals. The contribution from Ti 3d and Nb 4d orbitals is the lowest. This result clearly shows the high tendency of Fe for reducing during lithiation, which is validated by the CV analysis as well. Thus, the reduction sequence should be summarized as Fe → Ti → Nb.
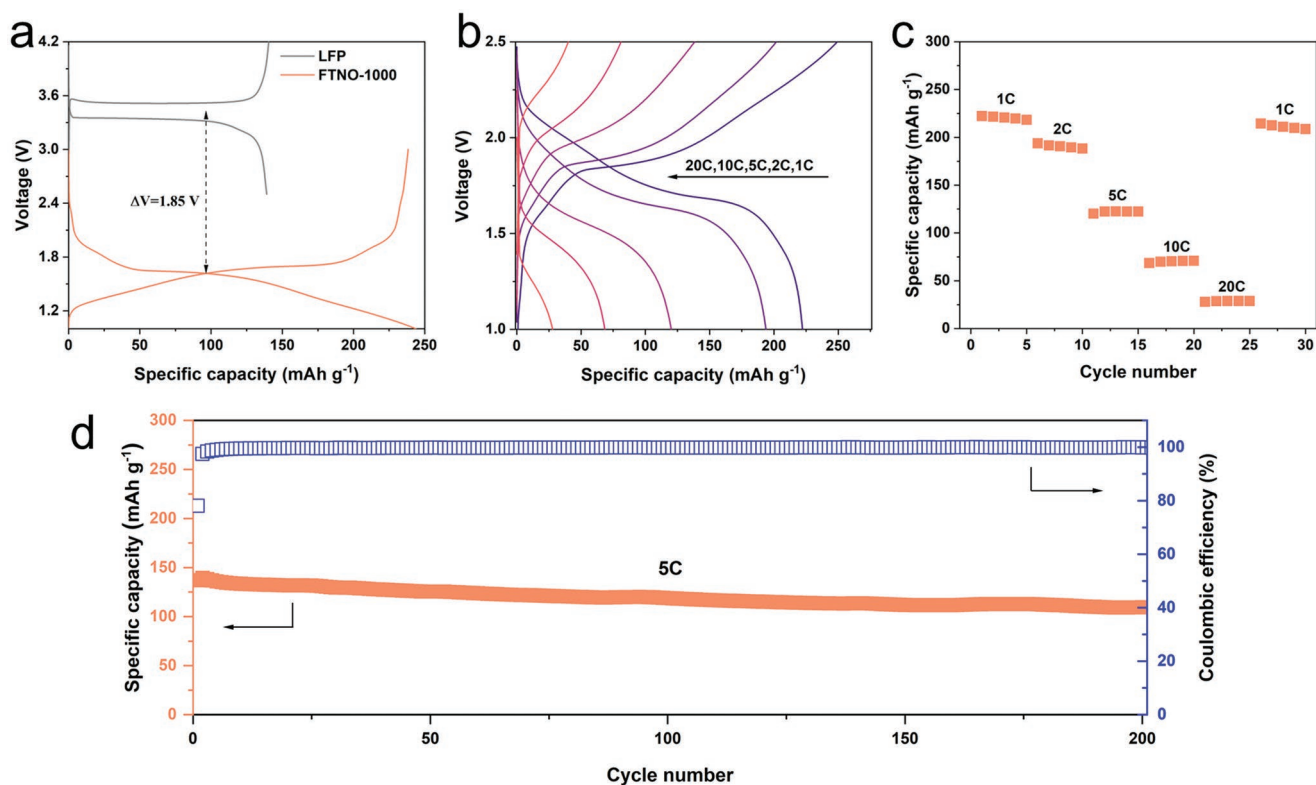
In this case, the lithiation-induced Δa and Δc of bare and Fe substitution cases during the first lithiation stage can be explained by the change in the length of Ti—O and Fe—O bonds that have large projections on the a– or c–axis (hereafter called Δl_a and Δl_c). As shown in **Figure 6**, when X increase to 1, the Δl_a for Ti—O in $Li_1Ti_2Nb_{10}O_{29}$ is ≈0.37 Å, while Δl_a for Fe—O in $Li_1Fe_1Ti_1Nb_{10}O_{28.5}$ is only ≈0.17 Å. The Δl_c for Ti—O in $Li_1Ti_2Nb_{10}O_{29}$ and Fe—O bonds in $Li_1Fe_1Ti_1Nb_{10}O_{28.5}$ are same (0.32 Å). The projected Δl_b on the b–axis remains almost unchanged in this lithiation stage. Based on above analysis, increasing entropy via iron substitution can stabilize the Wadsley–Roth phase by reducing the Δa value. It can be speculated that the continuously larger Δa of TNO-1100 would lead to structural instability along the a-direction, thus resulting in the observed capacity degradation during extensive cycling.

2.5. Practical Battery Performance

Based on the fact that FTNO-1000 electrodes present the best electrochemical performance in half cells among the three electrodes studied above, the potential of its practical application was investigated by assembling a full cell utilizing commercial $LiFePO_4$ cathode and the as-synthesized FTNO-1000 anode. The charge–discharged curves of a $LiFePO_4$ half cell exhibit a long plateau at ≈3.55 V (**Figure 7**a), while the main redox reaction of a FTNO-1000 half cell emerges at ≈1.7 V. Thus, the voltage range for the analysis of the $LiFePO_4\|FTNO$-1000 full cell was set to be ≈1.0–2.5 V. As the specific capacity of the commercial $LiFePO_4$ is 2 mAh cm^{-2}, a mass loading of 3.8 mg cm^{-2} for the FTNO-1000 electrode, (i.e., specific capacity of ≈1.0 mAh cm^{-2}), was applied for the full cell fabrication aiming to achieve capacity ratio of anode to cathode as ≈0.5. The initial charge–discharge curves of the $LiFePO_4\|FTNO$-1000 full cell at various C-rates are presented in Figure 7b. For the initial cycle at 1 C, the $LiFePO_4\|FTNO$-1000 full cell is able to deliver a charge and discharge capacity of 248.8 and 222.2 mAh g^{-1}, respectively, at the average working potential of ≈1.8 V, which is close to the expected voltage. For the following C-rates, the $LiFePO_4\|FTNO$-1000 full cell could exhibit a discharge capacity of 193.7, 122.4, 70.9, and 28.7 mAh g^{-1} at 2, 5, 10, and 20 C (Figure 7c). Furthermore, the cycling stability of the $LiFePO_4\|FTNO$-1000 full cell was investigated (Figure 7d). It is shown that a discharge capacity of 109.8 mAh g^{-1} with a
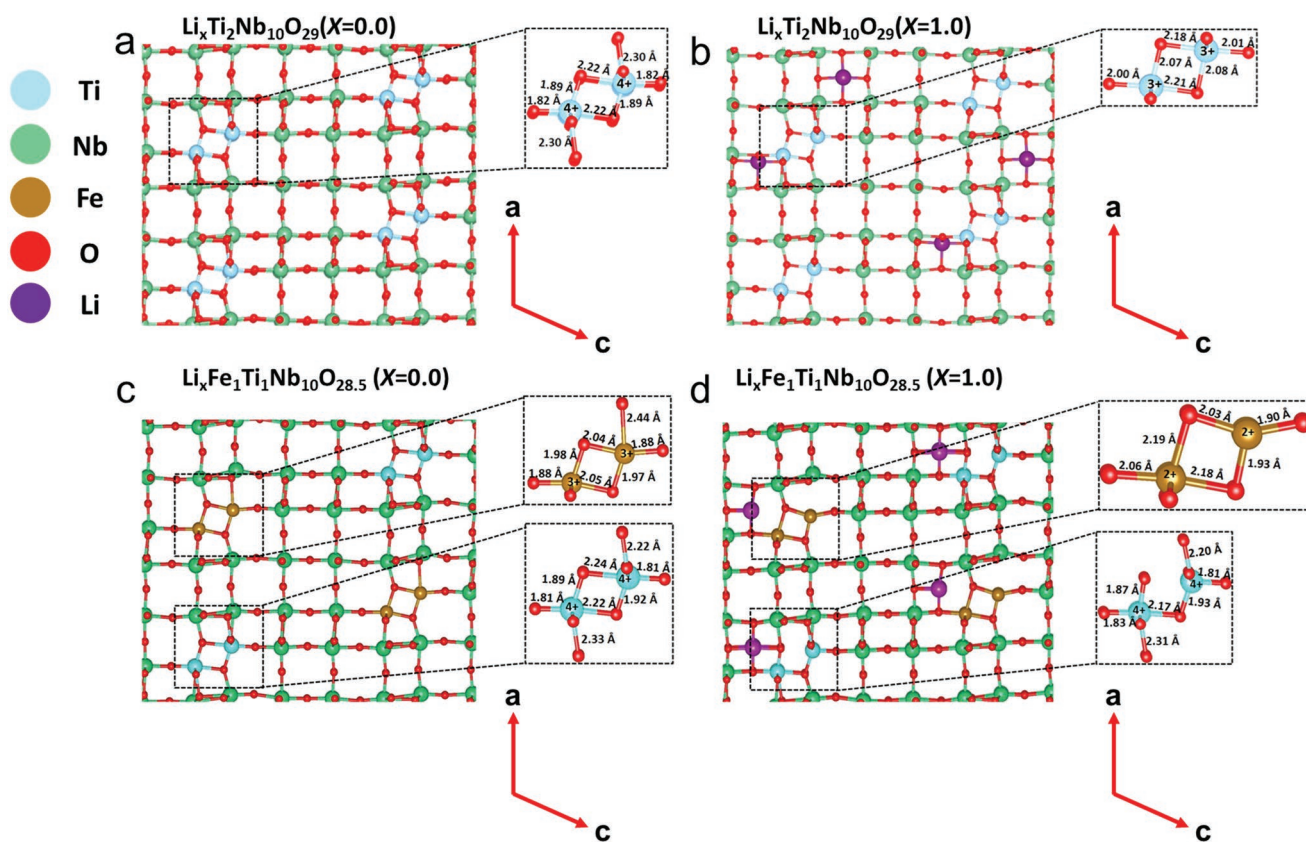
Figure 6. Calculated Ti—O and Fe—O bond length for a,b) $Li_xTi_2Nb_{10}O_{29}$ and c,d) $Li_xFe_1Ti_1Nb_{10}O_{28.5}$ before ($x = 0$) and after lithiation ($x = 1$).

ADVANCED
SCIENCE NEWS
www.advancedsciencenews.com

NANO · MICRO
small
www.small-journal.com

Figure 7. a) The charge–discharged curves of LiFePO₄ and FTNO-1000 in half cells; b) the charge–discharged curves and c) the specific capacity of LiFePO₄ ‖ FTNO-1000 full cell at various rates from 1 to 20 C; d) the long-term cycling performance of LiFePO₄‖FTNO-1000 full cell under 5 C. (1 C = 395 mA g⁻¹ and applying the mass of FTNO-1000 for the calculation of specific current density).

capacity retention of 80.3% could be achieved after 200 cycles at 5 C. Furthermore, the coulombic efficiency remains to be stable over 99.5% during most of the cycling process. Therefore, the FTNO-1000 electrode shows promising potential for practical applications when combined in full cells with commercial LiFePO₄ electrodes.

3. Conclusion

Fast and durable lithium storage performance in entropy-stabilized Wadsley–Roth phase FTNO has been successfully realized by tuning the entropy. Increasing the entropy by iron substitution leads to a reduction of the calcination temperature to 1000 °C to form a phase pure material, as compared to the required 1100 °C for the pristine compound. The lower formation temperature leads to the shortened Li⁺ diffusion channel length in FTNO-1000 due to the reduced grain size along the *b*-direction. Furthermore, the diffusion coefficient and the reaction rate constant are enhanced leading to a reduced overpotential and an improved rate performance. Benefiting from this, the micro-sized FTNO-1000 electrode exhibits an enhanced rate ability of 73.7 mAh g⁻¹ at 50 C as compared to 37.9 mAh g⁻¹ for its TNO counterpart. Furthermore, the increased entropy results in an extended cycling durability of FTNO demonstrated by operando XRD analysis that shows a suppression of the *a*–axis deformation during the first stage of the lithiation process. The mechanism is revealed by DFT calculations and found that Fe−O bond lengths undergo less changes than Ti−O during lithiation. Finally, the potential practical application of FTNO anodes has been demonstrated by successfully constructing fast charging and stable LiFePO₄‖FTNO full cells. This work provides a novel strategy by tuning entropy to stabilize the Wadsley–Roth phase with fast charging ability and can be extended to other intercalation electrodes for battery application.

4. Experimental Section

Material Synthesis: The solid-state reaction was applied to synthesize the TNO and FTNO powders using commercial TiO₂, Nb₂O₅, and Fe₂O₃ powders (Sigma Aldrich) as the raw materials. In detail, stoichiometric amounts of the raw materials (Ti:Nb = 1:5 for TNO, Ti:Nb:Fe = 0.4:1.6:10 for FTNO) were mixed by ball milling for 24 h, followed by calcination in a muffle oven at 1000 °C to obtain the TNO-1000, and FTNO-1000 powders, and at 1100 °C to get the TNO-1100 and FTNO-1100 powders. The heating rate was 5 °C min⁻¹ and the calcination duration was 20 h for all powders. The powders were cooled down to room temperature with cooling rate of 5 °C min⁻¹. All powders were annealed in a platinum crucible.

Material Characterization: The crystal information of all powders was collected by using XRD (PANalytical X'Pert PRO diffractometer with Cu Kα radiation, λ = 0.15406 nm). The thermal expansion behavior of the pristine mixture powder was recorded by dilatometry (NETZSCH, DIL 402C). The bonding characteristics were analyzed using Raman spectroscopy (1000 UV Raman spectrometer with laser wavelength of 514 nm for measurement). The elemental surface composition was

characterized by XPS (Omicron Nanotechnology GmbH surface analysis system with a photon energy of 1486.7 eV, Al $K\alpha$ X-ray source). The morphology of the powders was investigated by Scanning Electron Microscopy (Zeiss Merlin HRSEM). The atomic ratios of pristine and iron substituted FTNO were detected by X-ray fluorescence spectroscopy (XRF, Bruker S8 Tiger WDXRF with a Rhodium X-ray Tube). The surface area was characterized by applying the BET (Gemini VII of Micromeritics) technique. The atomic arrangement and crystal structure of FTNO and TNO were investigated by Scanning Transmission Electron Microscopy (STEM, Titan Themis TEM with CEOS probe and image aberration corrector operated at 200 KeV).

Electrochemical Analysis: The working electrodes were prepared by mixing the active materials, Super P and polyvinylidene difluoride (PVDF, Mw 27 500, Sigma Aldrich) with a mass ratio of 70:20:10. The FTNO-1000, FTNO-1100, or TNO-1100 powders were first ground with super P in an agate mortar for 15 min, followed by dispersion in *N*-methyl pyrrolidone (NMP, ≥ 99%, Sigma Aldrich) solution, which dissolved the PVDF with a concentration of 0.05 g mL^{-1}. Then ultrasonication was applied to treat the mixed slurry for 20 min. and the homogenous slurry was subsequently casted onto Cu foil. The prepared electrodes were dried in a vacuum oven for 12 h and the mass loading was ≈1.2 mg cm^{-2} for half cells ≈3.8 mg cm^{-2} for full cells, respectively. The half cells were assembled in a glove box applying the active materials electrode as cathode, lithium metal (99.9%, Sigma Aldrich) as anode, and glass fiber (ECC1-01-0012-B/L) as separator. The electrolyte was composed of 1.0 M LiPF$_6$ in 1:1 ratio v/v EC/DMC. As for the assembly of full cells, commercial LiFePO$_4$ was used as cathode while FTNO-1000 was used as anode. As the indicated capacity of the commercial LiFePO$_4$ electrode was 2 mAh cm^{-2}, a thick FTNO-1000 electrode with a higher mass loading of 3.8 mg cm^{-2} was applied to keep the capacity ratio of anode to cathode as ≈0.5. As for the operando XRD cell, the mass ratio of the mixed slurry was changed to 60:30:10 to achieve an enhanced electronic conductivity and the beryllium window was employed as current collector. All electrochemical measurements were conducted in a galvanostat/potentiostat (VMP-300, Biologic) with EC-Lab software at room temperature using commercial lab-scale cells (TU Delft).

Theoretical Modeling: Spin-polarized DFT calculations were performed using the projector augmented wave (PAW) potential method[66] implemented in the Vienna Ab Initio Simulation Package (VASP) code.[67] Generalized gradient approximation (GGA) within the scheme of Perdew–Burke–Ernzerhof (PBE)[68] was used as the basis of the exchange-correlation (XC) functional. The Hubbard correction proposed by Dudarev et al.[69] (U-J is simply presented by U hereafter) was considered to compute atomic coordinates, lattice parameters, and electronic structures. The following U values were applied: $U(Ti) = 3.0$ eV, $U(Nb) = 4.5$ eV, and $U(Fe) = 6.0$ eV. A k-point mesh of $1 \times 4 \times 1$ and an energy cut off of 520 eV as well as an electronic and a force convergence criterion of 10^{-4} eV and 10^{-3} eV Å^{-1}, respectively, were considered. Magnetic moments (number of unpaired electrons) were, however, calculated using a tighter electronic and force convergence criterion of 10^{-6} eV and 10^{-5} eV Å^{-1}, respectively. The most favorable atomic configuration for each system was determined by performing an extensive set of Coulomb energy calculations (using the so-called supercell code[70]) to find the lowest-electrostatic energy structure. The number of considered structures and charges on ions are discussed in the following. To find the preferred occupation site for Ti in Nb$_{12}$O$_{29}$ (modeled by Nb$_{24}$O$_{58}$) to study Ti$_2$Nb$_{10}$O$_{29}$ the Coulomb energy (E_C) of all possible configurations was computed with 4 Ti ions in 24 Nb sites, namely $\frac{24!}{4!20!} = 10\,626$ structures. For charge balancing, charges of 4+ for Ti, 5+ for Nb, and 2− for O were used. To find the most favorable site for 2 Li ions in Ti$_2$Nb$_{10}$O$_{29}$ (modeled by Li$_2$Ti$_4$Nb$_{20}$O$_{58}$), all possible configurations were considered with 2 Li$^+$ in 45 possible interstitial sites (with a minimum distance of 1.9 Å with respect to nearest neighbor ions) as well as 2 Ti^{3+} and 2 Ti^{4+} in 4 Ti sites, namely, $\frac{45!}{2!43!} \cdot \frac{4!}{2!2!} = 5940$ structures. E_C values of 5940 structures were obtained using elementary charges of 1+ for Li, 5+ for Nb, and 2− for

O. The Fe-substitution system was modeled with an oxygen vacancy (V_O^x) in Ti$_2$Fe$_2$Nb$_{20}$O$_{57}$ and Li$_2$Ti$_2$Fe$_2$Nb$_{20}$O$_{57}$. All possible configurations were considered with 2 Fe ions in 4 Ti-sites and 1 oxygen ion vacancy in 58 oxygen sites, $\frac{4!}{2!2!} \cdot \frac{58!}{1!57!} = 348$ structures. Elementary charges of 4+ for Ti, 3+ for Fe, 5+ for Nb, and 2− for O were used. Finally, DFT-PBE calculation was performed on the structure with the lowest E_C for each system and the optimized geometry of each case was used to perform DFT-PBE+U calculation. The atomistic structures were visualized with the VESTA program.[71]

Supporting Information

Supporting Information is available from the Wiley Online Library or from the author.

Conflict of Interest

The authors declare no conflict of interest.

Data Availability Statement

The data that support the findings of this study are available from the corresponding author upon reasonable request.

[1] Y. Liu, Y. Zhu, Y. Cui, *Nat. Energy* **2019**, *4*, 540.
[2] M. Weiss, R. Ruess, J. Kasnatscheew, Y. Levartovsky, N. R. Levy, P. Minnmann, L. Stolz, T. Waldmann, M. Wohlfahrt-Mehrens, D. Aurbach, M. Winter, Y. Ein-Eli, J. Janek, *Adv. Energy Mater.* **2021**, *11*, 2101126.
[3] K. J. Griffith, K. M. Wiaderek, G. Cibin, L. E. Marbella, C. P. Grey, *Nature* **2018**, *559*, 556.
[4] Y. Yang, H. Zhu, J. Xiao, H. Geng, Y. Zhang, J. Zhao, G. Li, X. L. Wang, C. C. Li, Q. Liu, *Adv. Mater.* **2020**, *32*, 1905295.
[5] R. Xia, K. Zhao, L. Y. Kuo, L. Zhang, D. M. Cunha, Y. Wang, S. Huang, J. Zheng, B. Boukamp, P. Kaghazchi, C. Sun, J. E. ten Elshof, M. Huijben, *Adv. Energy Mater.* **2022**, *12*, 2102972.
[6] Y. Yang, J. Zhao, *Adv. Sci.* **2021**, *8*, 2004855.
[7] X. Wu, J. Miao, W. Han, Y.-S. Hu, D. Chen, J.-S. Lee, J. Kim, L. Chen, *Electrochem. Commun.* **2012**, *25*, 39.

[8] Q. Cheng, J. Liang, Y. Zhu, L. Si, C. Guo, Y. Qian, *J. Mater. Chem. A* **2014**, *2*, 17258.

[9] L. Shen, E. Uchaker, X. Zhang, G. Cao, *Adv. Mater.* **2012**, *24*, 6502.

[10] L. Aldon, P. Kubiak, M. Womes, J. Jumas, J. Olivier-Fourcade, J. Tirado, J. Corredor, C. P. Vicente, *Chem. Mater.* **2004**, *16*, 5721.

[11] J. Asenbauer, T. Eisenmann, M. Kuenzel, A. Kazzazi, Z. Chen, D. Bresser, *Sustainable Energy Fuels* **2020**, *4*, 5387.

[12] J. B. Goodenough, Y. Kim, *Chem. Mater.* **2010**, *22*, 587.

[13] X. Wang, J. Feng, Y. Bai, Q. Zhang, Y. Yin, *Chem. Rev.* **2016**, *116*, 10983.

[14] H. Geng, Y. Peng, L. Qu, H. Zhang, M. Wu, *Adv. Energy Mater.* **2020**, *10*, 1903030.

[15] M. F. Oszajca, M. I. Bodnarchuk, M. V. Kovalenko, *Chem. Mater.* **2014**, *26*, 5422.

[16] C. Lin, G. Wang, S. Lin, J. Li, L. Lu, *Chem. Commun.* **2015**, *51*, 8970.

[17] T. Yuan, L. Soule, B. Zhao, J. Zou, J. Yang, M. Liu, S. Zheng, *Energy Fuels* **2020**, *34*, 13321.

[18] T. Yuan, S. Luo, L. Soule, J.-H. Wang, Y. Wang, D. Sun, B. Zhao, W. Li, J. Yang, S. Zheng, M. Liu, *Mater. Today* **2021**, *45*, 8.

[19] C. Lin, S. Yu, H. Zhao, S. Wu, G. Wang, L. Yu, Y. Li, Z.-Z. Zhu, J. Li, S. Lin, *Sci. Rep.* **2015**, *5*, 17836.

[20] C. Lin, S. Yu, S. Wu, S. Lin, Z.-Z. Zhu, J. Li, L. Lu, *J. Mater. Chem. A* **2015**, *3*, 8627.

[21] C. Yang, S. Yu, Y. Ma, C. Lin, Z. Xu, H. Zhao, S. Wu, P. Zheng, Z.-Z. Zhu, J. Li, N. Wang, *J. Power Sources* **2017**, *360*, 470.

[22] C. Yang, C. Lin, S. Lin, Y. Chen, J. Li, *J. Power Sources* **2016**, *328*, 336.

[23] Z. Wu, M. Guo, Y. Yan, H. Dou, W. Zhao, Y. Zhang, S. Li, J. Wu, X. Bin, X. Zhao, X. Yang, D. Ruan, *ACS Sustainable Chem. Eng.* **2021**, *9*, 7422.

[24] Z. Lv, H. Zhu, W. Meng, L. Wei, Y. Yang, Y. Zhang, M. Ye, C. C. Li, *Appl. Phys. Rev.* **2021**, *8*, 031404.

[25] Y. Zeng, B. Ouyang, J. Liu, Y.-W. Byeon, Z. Cai, L. J. Miara, Y. Wang, G. Ceder, *Science* **2022**, *378*, 1320.

[26] R. Zhang, C. Wang, P. Zou, R. Lin, L. Ma, L. Yin, T. Li, W. Xu, H. Jia, Q. Y. Li, S. Sainio, K. Kisslinger, S. E. Trask, S. N. Ehrlich, Y. Yang, A. M. Kiss, M. Ge, B. J. Polzin, S. J. Lee, W. Xu, Y. Ren, H. L. Xin, *Nature* **2022**, *610*, 67.

[27] Y. Ma, Y. Hu, Y. Pramudya, T. Diemant, Q. Wang, D. Goonetilleke, Y. Tang, B. Zhou, H. Hahn, W. Wenzel, M. Fichtner, Y. Ma, B. Breiting, T. Brezesinski, *Adv. Funct. Mater.* **2022**, *32*, 2202372.

[28] A. A. Voskanyan, M. Abramchuk, A. Navrotsky, *Chem. Mater.* **2020**, *32*, 5301.

[29] K. J. Griffith, I. D. Seymour, M. A. Hope, M. M. Butala, L. K. Lamontagne, M. B. Preefer, C. P. Koçer, G. Henkelman, A. J. Morris, M. J. Cliffe, S. E. Dutton, C. P. Grey, *J. Am. Chem. Soc.* **2019**, *141*, 16706.

[30] C. M. Rost, E. Sachet, T. Borman, A. Moballegh, E. C. Dickey, D. Hou, J. L. Jones, S. Curtarolo, J.-P. Maria, *Nat. Commun.* **2015**, *6*, 8485.

[31] A. Sarkar, Q. Wang, A. Schiele, M. R. Chellali, S. S. Bhattacharya, D. Wang, T. Brezesinski, H. Hahn, L. Velasco, B. Breitung, *Adv. Mater.* **2019**, *31*, 1806236.

[32] T. Li, G. Nam, K. Liu, J.-H. Wang, B. Zhao, Y. Ding, L. Soule, M. Avdeev, Z. Luo, W. Zhang, T. Yuan, P. Jing, M. G. Kim, Y. Song, M. Liu, *Energy Environ. Sci.* **2022**, *15*, 254.

[33] R. D. Shannon, *Acta Crystallogr., Sect. A: Found. Adv.* **1976**, *32*, 751.

[34] A. Patterson, *Phys. Rev.* **1939**, *56*, 972.

[35] A. K. Zak, W. H. Abd. Majid, M. E. Abrishami, R. Yousefi, *Solid State Sci.* **2011**, *13*, 251.

[36] A. Nie, L. Y. Gan, Y. Cheng, Q. Li, Y. Yuan, F. Mashayek, H. Wang, R. Klie, U. Schwingenschlog, R. Shahbazian-Yassar, *Nano Lett.* **2015**, *15*, 610.

[37] X. Xiong, L. Yang, G. Liang, C. Wang, G. Chen, Z. Yang, R. Che, *Adv. Funct. Mater.* **2022**, *32*, 2106911.

[38] S. Lou, X. Cheng, J. Gao, Q. Li, L. Wang, Y. Cao, Y. Ma, P. Zuo, Y. Gao, C. Du, H. Huo, G. Yin, *Energy Storage Mater.* **2018**, *11*, 57.

[39] D. Spada, M. C. Mozzati, B. Albini, P. Galinetto, I. Quinzeni, D. Capsoni, M. Bini, *Dalton Trans.* **2018**, *47*, 15816.

[40] S. Deng, Z. Luo, Y. Liu, X. Lou, C. Lin, C. Yang, H. Zhao, P. Zheng, Z. Sun, J. Li, N. Wang, H. Wu, *J. Power Sources* **2017**, *362*, 250.

[41] R. B. V. Dreele, A. K. Cheetham, *Proc. R. Soc. A* **1974**, *338*, 311.

[42] D. Spada, I. Quinzeni, M. Bini, *Electrochim. Acta* **2019**, *296*, 938.

[43] R. Zheng, S. Qian, X. Cheng, H. Yu, N. Peng, T. Liu, J. Zhang, M. Xia, H. Zhu, J. Shu, *Nano Energy* **2019**, *58*, 399.

[44] B. Guo, X. Yu, X. G. Sun, M. Chi, Z. A. Qiao, J. Liu, Y. S. Hu, X. Q. Yang, J. B. Goodenough, S. Dai, *Energy Environ. Sci.* **2014**, *7*, 2220.

[45] X. Xia, S. Deng, S. Feng, J. Wu, J. Tu, *J. Mater. Chem. A* **2017**, *5*, 21134.

[46] W. L. Wang, B.-Y. Oh, J.-Y. Park, H. Ki, J. Jang, G.-Y. Lee, H.-B. Gu, M.-H. Ham, *J. Power Sources* **2015**, *300*, 272.

[47] M. Inaba, Y. Oba, F. Niina, Y. Murota, Y. Ogino, A. Tasaka, K. Hirota, *J. Power Sources* **2009**, *189*, 580.

[48] H.-G. Jung, S.-T. Myung, C. S. Yoon, S.-B. Son, K. H. Oh, K. Amine, B. Scrosati, Y.-K. Sun, *Environ. Sci.* **2011**, *4*, 1345.

[49] H. Sun, L. Mei, J. Liang, Z. Zhao, C. Lee, H. Fei, M. Ding, J. Lau, M. Li, C. Wang, X. Xu, G. Hao, B. Papandrea, I. Sharkir, B. Dunn, Y. Huang, X. Duan, *Science* **2017**, *356*, 599.

[50] Y. Zhang, M. Zhang, Y. Liu, H. Zhu, L. Wang, Y. Liu, M. Xue, B. Li, X. T. Tao, *Electrochim. Acta* **2020**, *330*, 135299.

[51] X. Z. Li, N. Zhang, Y. R. Wu, Q. Z. Lai, Y. R. Zhu, J. H. Zhang, P. Cui, T. F. Yi, *Rare Met.* **2022**, *41*, 3401.

[52] S. L. Cheng, X. P. Yin, S. Sarkar, Z. W. Wang, Q. A. Huang, J. J. Zhang, Y. F. Zhao, *Rare Met.* **2022**, *41*, 2645.

[53] Z. Liu, W. Dong, J. Wang, C. Dong, Y. Lin, I.-W. Chen, F. Huang, *iScience* **2020**, *23*, 100767.

[54] H. Zhang, R. Hu, S. Feng, Z. Lin, M. Zhu, *eScience* **2023**, *3*, 100080.

[55] W. Dong, Y. Zhao, X. Wang, X. Yuan, K. Bu, C. Dong, R. Wang, F. Huang, *Adv. Mater.* **2018**, *30*, 1801409.

[56] W. Dong, R. Li, J. Xu, Y. Tang, F. Huang, *Cell Rep. Phys. Sci.* **2022**, *3*, 101109.

[57] W. Dong, Y. Zhao, M. Cai, C. Dong, W. Ma, J. Pan, Z. Lv, H. Dong, Y. Dong, Y. Tang, F. Huang, *Small* **2023**, 2207074.

[58] C. Lin, L. Hu, C. Cheng, K. Sun, X. Guo, Q. Shao, J. Li, N. Wang, Z. Guo, *Electrochim. Acta* **2018**, *260*, 65.

[59] R. Xia, K. Zhao, J. Zheng, T. Shen, L. Zhang, M. Huijben, J. E. ten Elshof, *Energy Storage Mater.* **2022**, *53*, 381.

[60] M. Nakayama, H. Ikuta, Y. Uchimoto, M. Wakihara, *J. Phys. Chem. B* **2003**, *107*, 10603.

[61] X. Lou, C. Lin, Q. Luo, J. Zhao, B. Wang, J. Li, Q. Shao, X. Guo, N. Wang, Z. Guo, *ChemElectroChem* **2017**, *4*, 3171.

[62] H. Yu, H. Lan, L. Yan, S. Qian, X. Cheng, H. Zhu, N. Long, M. Shui, J. Shu, *Nano Energy* **2017**, *38*, 109.

[63] H. Yu, X. Cheng, H. Zhu, R. Zheng, T. Liu, J. Zhang, M. Shui, Y. Xie, J. Shu, *Nano Energy* **2018**, *54*, 227.

[64] X. Lu, Z. Jian, Z. Fang, L. Gu, Y.-S. Hu, W. Chen, Z. Wang, L. Chen, *Energy Environ. Sci.* **2011**, *4*, 2638.

[65] S. Deng, H. Zhu, G. Wang, M. Luo, S. Shen, C. Ai, L. Yang, S. Lin, Q. Zhang, L. Gu, B. Liu, Y. Zhang, Q. Liu, G. Pan, Q. Xiong, X. Wang, X. Xia, J. Tu, *Nat. Commun.* **2020**, *11*, 132.

[66] P. E. Blöchl, *Phys. Rev. B* **1994**, *50*, 17953.

[67] G. Kresse, J. Furthmüller, *Phys. Rev. B* **1996**, *54*, 11169.

[68] J. P. Perdew, K. Burke, M. Ernzerhof, *Phys. Rev. Lett.* **1996**, *77*, 3865.

[69] S. L. Dudarev, G. A. Botton, S. Y. Savrasov, C. J. Humphreys, A. P. Sutton, *Phys. Rev. B* **1998**, *57*, 1505.

[70] K. Okhotnikov, T. Charpentier, S. Cadars, *J. Cheminf.* **2016**, *8*, 17.

[71] K. Momma, F. Izumi, *J. Appl. Crystallogr.* **2011**, *44*, 1272.